JOPSS
JAEA Originated Papers Searching System

日本原子力研究開発機構機関リポジトリ
Japan Atomic Energy Agency Institutional Repository

Title	Fast magnetic field annihilation driven by two laser pulses in underdense plasma
Author(s)	Gu Y. J., Klimo O., Kumar D., Bulanov S. V., Esirkepov T. Z., Weber S., Korn G.
Citation	Physics of Plasmas, 22(10), p.103113_1-103113_9
Text Version	Publisher's Version
URL	https://jopss.jaea.go.jp/search/servlet/search?5053704
DOI	https://doi.org/10.1063/1.4933408
Right	This article may be downloaded for personal use only. Any other use requires prior permission of the author and the American Institute of Physics. The following article appeared in Physics of Plasmas and may be found at https://doi.org/10.1063/1.4933408.

Japan Atomic Energy Agency

Fast magnetic field annihilation driven by two laser pulses in underdense plasma

Y. J. Gu, O. Klimo, D. Kumar, S. V. Bulanov, T. Zh. Esirkepov, S. Weber, and G. Korn

Citation: Physics of Plasmas **22**, 103113 (2015); doi: 10.1063/1.4933408
View online: http://dx.doi.org/10.1063/1.4933408
View Table of Contents: http://scitation.aip.org/content/aip/journal/pop/22/10?ver=pdfcov
Published by the AIP Publishing

Articles you may be interested in

The effect of external magnetic field on the bremsstrahlung nonlinear absorption mechanism in the interaction of high intensity short laser pulse with collisional underdense plasma
Phys. Plasmas **22**, 033114 (2015); 10.1063/1.4916127

Use of external magnetic fields in hohlraum plasmas to improve laser-coupling
Phys. Plasmas **22**, 010703 (2015); 10.1063/1.4906055

Axial magnetic field generation by intense circularly polarized laser pulses in underdense plasmas
Phys. Plasmas **17**, 083109 (2010); 10.1063/1.3471940

Plasma wake inhibition at the collision of two laser pulses in an underdense plasma
Phys. Plasmas **14**, 060702 (2007); 10.1063/1.2741387

Ion momentum driven by a short intense laser pulse in an underdense plasma
Phys. Plasmas **7**, 375 (2000); 10.1063/1.873806

This article is copyrighted as indicated in the article. Reuse of AIP content is subject to the terms at: http://scitation.aip.org/termsconditions. Downloaded to IP: 61.86.248.29 On: Mon, 19 Oct 2015 20:10:37

Fast magnetic field annihilation driven by two laser pulses in underdense plasma

Y. J. Gu,[1] O. Klimo,[1,2] D. Kumar,[1] S. V. Bulanov,[3] T. Zh. Esirkepov,[3] S. Weber,[1] and G. Korn[1]
[1]*Institute of Physics of the ASCR, ELI-Beamlines, 18221 Prague, Czech Republic*
[2]*FNSPE, Czech Technical University in Prague, 11519 Prague, Czech Republic*
[3]*Kansai Photon Science Institute, Japan Atomic Energy Agency, 8-1-7 Umemidai, Kizugawa-shi, Kyoto 619-0215, Japan*

(Received 2 August 2015; accepted 6 October 2015; published online 19 October 2015)

Fast magnetic annihilation is investigated by using 2.5-dimensional particle-in-cell simulations of two parallel ultra-short petawatt laser pulses co-propagating in underdense plasma. The magnetic field generated by the laser pulses annihilates in a current sheet formed between the pulses. Magnetic field energy is converted to an inductive longitudinal electric field, which efficiently accelerates the electrons of the current sheet. This new regime of collisionless relativistic magnetic field annihilation with a timescale of tens of femtoseconds can be extended to near-critical and overdense plasma with the ultra-high intensity femtosecond laser pulses. © *2015 AIP Publishing LLC*.
[http://dx.doi.org/10.1063/1.4933408]

I. INTRODUCTION

Fast magnetic field dissipation via magnetic line reconnection or magnetic field annihilation is a fundamental phenomenon in space and laboratory plasmas.[1–4] It is accompanied by a conversion of the magnetic field energy into fast charged particles causing plasma heating. In both astrophysics[5,6] and laboratory plasma physics,[7] magnetic reconnection participates in many processes, exemplified by solar flares,[8–10] coronal mass ejections,[11,12] open and closed planetary magnetosphere,[13,14] γ-ray bursts,[15–18] and fusion plasma instabilities.[19,20] The corresponding theoretical and experimental studies have been presented and reviewed in many papers.[21–25]

With the rapid development of high power laser technology,[26] multipetawatt lasers are available nowadays which make it possible to investigate fast magnetic field dissipation using laser-plasma interactions.[27] Fast electron current generation in relativistic laser plasmas and their interactions via magnetic fields were first proposed by Askar'yan *et al.*[28] In the pioneering experimental work by Nilson *et al.*,[29] two nanosecond laser beams were focused on a planar solid target inducing mega-gauss magnetic fields at the focal point edges. The high temperature of electrons (1.7 keV) and plasma jets observed in the experiment were consistent with the signatures of magnetic reconnection. Li *et al.*[30] irradiated a thin plastic (CH) foil with two or four 1-ns long OMEGA laser beams. Magnetic fields and the corresponding topological changes due to reconnection were directly measured using time-resolved proton deflection technique. Recently, Zhong *et al.*[31] demonstrated a loop-top X-ray source by using reconnection outflows. Four synchronized nanosecond laser beams were symmetrically focused on both sides of an aluminum solid foil. Mega-gauss magnetic fields, high energy plasmas, and a magnetic reconnection topology related to solar flares were observed. A similar laser setup was used to irradiate two separated Al foils by Dong *et al.*[32] Fan-like plasma outflows with MeV electrons and a plasmoid were generated and ejected from the current sheet during magnetic reconnection. Energy transfer from the laser-produced magnetic field to plasma particles has also been studied by Kawata *et al.*[33,34] The inductive electric field generated by the magnetic field accelerates ions to high energy. In addition, other theoretical and experimental works used long pulse duration laser beams and solid targets to investigate magnetic reconnection.[35–39]

Theoretical studies and simulations using magnetohydrodynamic (MHD) codes analyze magnetic reconnections in a number of papers.[40–44] A lot of work investigating magnetic reconnection explained the corresponding mechanisms with the help of particle-in-cell (PIC) simulations.[45–56] Olshevsky *et al.*[57] performed three-dimensional (3D) PIC simulations of a cluster with preformed null points and fully periodic boundaries. They discussed the microphysics of magnetic reconnection using a small simulation box observing that more than 85% of the magnetic field energy is converted to particle kinetic energy.

The research of laser-plasma induced fast magnetic field dissipation has attracted significant interest recently. However, most of the simulations do not include the laser-plasma interaction stages, assuming the initial conditions where bubble structures with high energy electron currents start to evolve in a cold background plasma. This might be due to a lack of computer resources, since the time scale of the laser plasma evolution before the onset of magnetic reconnection is of the order of nano-second. In contrast, Ping *et al.*[58] reported a fast reconnection driven by two ultra-intense laser pulses using 3D PIC simulations. The fast magnetic reconnection was achieved within 50 laser periods, and the corresponding change of the topology structure was observed.

In this paper, we investigate fast magnetic field dissipation in the interaction of two parallel synchronized ultra-intense and ultra-short s-polarized laser pulses co-propagating in underdense plasmas. Our 2.5-dimensional PIC simulations emphasize the magnetic field annihilation, a particular mode

 © 2015 AIP Publishing LLC

This article is copyrighted as indicated in the article. Reuse of AIP content is subject to the terms at: http://scitation.aip.org/termsconditions. Downloaded to IP: 61.86.248.29 On: Mon, 19 Oct 2015 20:10:37

of the fast magnetic field dissipation, leaving the magnetic line reconnection undetectable due to symmetry. Here, the low dimension geometry allows the properties of the magnetic annihilation to be distinctly seen. In contrast to previous publications with nanosecond or picosecond pulses, in our simulations, the laser pulses are as short as tens of femtoseconds. Magnetic dipoles generated by two parallel laser pulses transversely expand in a low-density plasma, touching each other at the axis between the laser beams. There a current sheet is formed which initially balances the curl of the magnetic field. When the transverse gradient of the magnetic field increases, the current sheet can no longer sustain the magnetic field, because the electric current is limited by the condition that the electrons cannot move faster than light in vacuum. Then, converging regions of opposite magnetic field annihilate, producing a displacement current which balances the curl of the magnetic field. The corresponding inductive electric field directed along the current sheet accelerates charged particles. In this way, large-scale magnetic field energy is converted into fast particles on a timescale of few tens of femtosecond. We also discuss the effects of laser parameters, including the separation distance between two pulses, and plasma density on the rate of magnetic annihilation. Our study opens a way for experimental realization of fast magnetic field dissipation via magnetic annihilation and magnetic line reconnection with ultra-intense and ultra-short laser pulses using the future multi-petawatt laser facility such as ELI-Beamlines.[59]

II. SIMULATION MODEL

We perform PIC simulations with the relativistic electromagnetic code EPOCH.[60] Hydrogen plasma with the peak density of $0.1\,n_c$, where n_c is the plasma critical density, occupies the region defined as $20\lambda < x < 122\lambda$ and $-20\lambda < y < 20\lambda$ in the simulation box, which has the size of 195λ and 340λ in the x and y direction, respectively. Here, λ is the laser wavelength, which is assumed to be $\lambda = 1\ \mu$m. Plasma represented by 10^7 quasiparticles is uniform in the y direction and non-uniform in the x direction as shown in Fig. 1(a). Along the x direction, the density profile linearly increases to $0.1n_c$ within 2λ, then remains constant for 40 λ, and finally linearly decreases to zero in a long downramp from 62λ to 122λ. Two s-polarized laser pulses with peak intensity of $10^{21}\,\mathrm{W/cm^2}$ are focused on the left boundary of the target with the spot size of 3λ. Each pulse has the Gaussian profile given by

$$a = a_0 \exp\left[-\left(\frac{t-\tau}{0.5\tau}\right)^2\right], \tag{1}$$

where $a_0 = eE_0/m_e\omega c \approx 27$ is the normalized amplitude, the pulse duration is $\tau = 15$ fs, E_0 and ω are the laser electric field strength and frequency, e and m_e are the electron charge and mass, respectively, and c is the speed of light in vacuum. The optical axes of two laser pulses are transversely separated by 14λ, being at $y = \pm 7\lambda$. Open boundary conditions are employed for both particles and fields in all directions. The simulation box transverse size is chosen to be large enough to weaken the unphysical boundary effects. The mesh size is $\delta x = \delta y = \lambda/20$. The timestep is $0.03\lambda/c$. All the quasiparticles are initially at rest, amounting to 16 quasiparticles per cell.

III. THE RESULTS OF 2D PIC SIMULATIONS

A. Magnetic dipoles generation, magnetic field annihilation, and charged particle acceleration

When the laser pulses propagate in a plasma, some of the electrons are expelled away from the region occupied by the laser pulses leading to the formation of bubble structures.

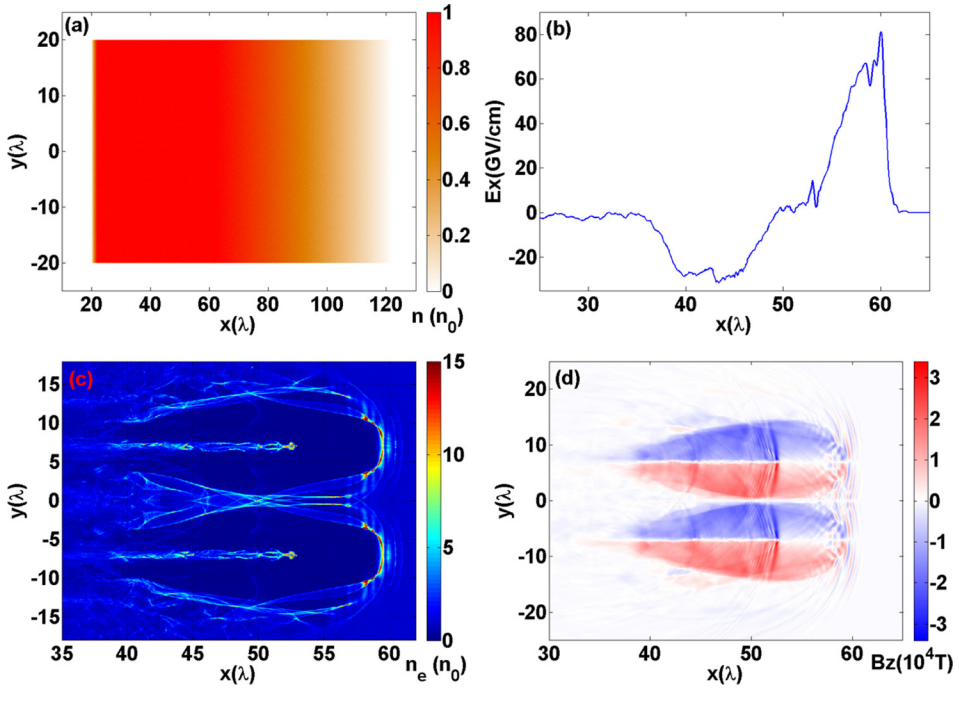

FIG. 1. (a) The initial density distribution of the target. (b) The longitudinal electric field (E_x) distribution along one of the laser axes, $y = 7\lambda$, at $t = 63\,T_0$. (c) Distribution of electron density normalized by the initial density $n_0 = 0.1n_c$ at $t = 63\,T_0$. (d) The corresponding z-component of the magnetic field (B_z) distribution.

This article is copyrighted as indicated in the article. Reuse of AIP content is subject to the terms at: http://scitation.aip.org/termsconditions. Downloaded to IP: 61.86.248.29 On: Mon, 19 Oct 2015 20:10:37

A strong wakefield is excited behind each laser pulse. The maximum amplitude of the wakefield is given by Sprangle *et al.*[61] as

$$E_{max} = 0.38\frac{2\gamma}{\sqrt{1+\gamma}}\sqrt{n_0}, \tag{2}$$

which is approximately 34 GV/cm in our case; γ is the electron relativistic factor. The wakefield amplitude in our simulation agrees well with the theoretical estimate as shown in Fig. 1(b). A bunch of electrons is trapped and accelerated by the wakefield up to several tens of MeV within tens of μm. The electron density distribution at $t = 63\,T_0$ is plotted in Fig. 1(c), where $T_0 = \lambda/c$ is the laser period. Two bubbles, each containing an accelerated electron bunch, propagate forward with the group velocity of the laser pulse. At this moment shown in Fig. 1(c), the parallel electron bunches moving in the bubbles are quasi-monoenergetic with the peak energy about 48 MeV, each containing a charge of about 1 nC/μm. The bunch energy spread is about $\delta E/E \approx 6.25\%$. The electron bunches are further accelerated in the later stages reaching the maximum energy of 120 MeV before they exit the target. The electric currents of the bubble produce magnetic fields according to Ampère-Maxwell law. The azimuthal field component B_θ with respect to the x axis is represented in the 2D configuration by the component B_z perpendicular to the plane. Therefore, two symmetric structures shown in Fig. 1(d) correspond to two magnetic dipoles, nearly touching the central axis at $y = 0$. The maximum magnetic field can be calculated by Ampère-Maxwell equation as

$$\nabla \times \mathbf{B} = \mu_0 \mathbf{J_e} + \mu_0 \varepsilon_0 \frac{\partial \mathbf{E}}{\partial t}. \tag{3}$$

Assuming the quasistatic condition ($\partial E/\partial t = 0$) and estimating the radius of the magnetic dipole as

$$R \approx c\sqrt{a_0}/\omega_p, \tag{4}$$

we obtain the magnitude of B_z as[62]

$$B_z = \mu_0 n_0 e c^2 \frac{\sqrt{\gamma}}{\omega_p} \approx 1.8 \times 10^4 \mathrm{T}, \tag{5}$$

which is in agreement with the distribution shown in Fig. 1(d).

In the inhomogeneous density region (i.e., downramp), the electron bubbles experience forces proportional to $\nabla n \times \Omega$, where ∇n is the density gradient, and $\Omega_z = B_z - (c/\omega_{pe})^2 \Delta B_z$ is the potential vorticity in the framework of electron magnetohydrodynamics (EMHD).[63,64] Therefore, the bubbles expand in the transverse direction together with the magnetic dipoles. The electron density distributions at 75 T_0, 87 T_0, and 99 T_0 are depicted in Figs. 2(a), 2(b), and 2(c), respectively. The transverse size of the bubbles increased from $\pm 15\,\lambda$ to $\pm 20\,\lambda$ as shown in the figures. The corresponding current density is plotted in Figs. 2(d)–2(f). The distribution of the return currents coincides with the expanding bubble boundaries. At the same time, the intensity of the current gradually decreases in time. This is due to the decrease of the electron density in the downramp. Correspondingly, the magnetic field in the bubbles becomes weaker while the area it covers increases, according to Ertel's theorem.[65]

In Figs. 3(a) and 3(b), we present the distribution of the z-component of the magnetic fields at 123 T_0 and 153 T_0, respectively. The transverse size of the magnetic field increases from $\pm 20\,\lambda$ to more than $\pm 30\,\lambda$, while the inner dipole in the stripe $-5\lambda < y < 5\lambda$ near the central axis ($y = 0$) becomes narrower. In this inner dipole, the magnetic fields with opposite direction annihilate. At 123 T_0, a part of the magnetic field has already been annihilated. In the vicinity of the central axis, a current sheet is formed, where the electric current is perpendicular to

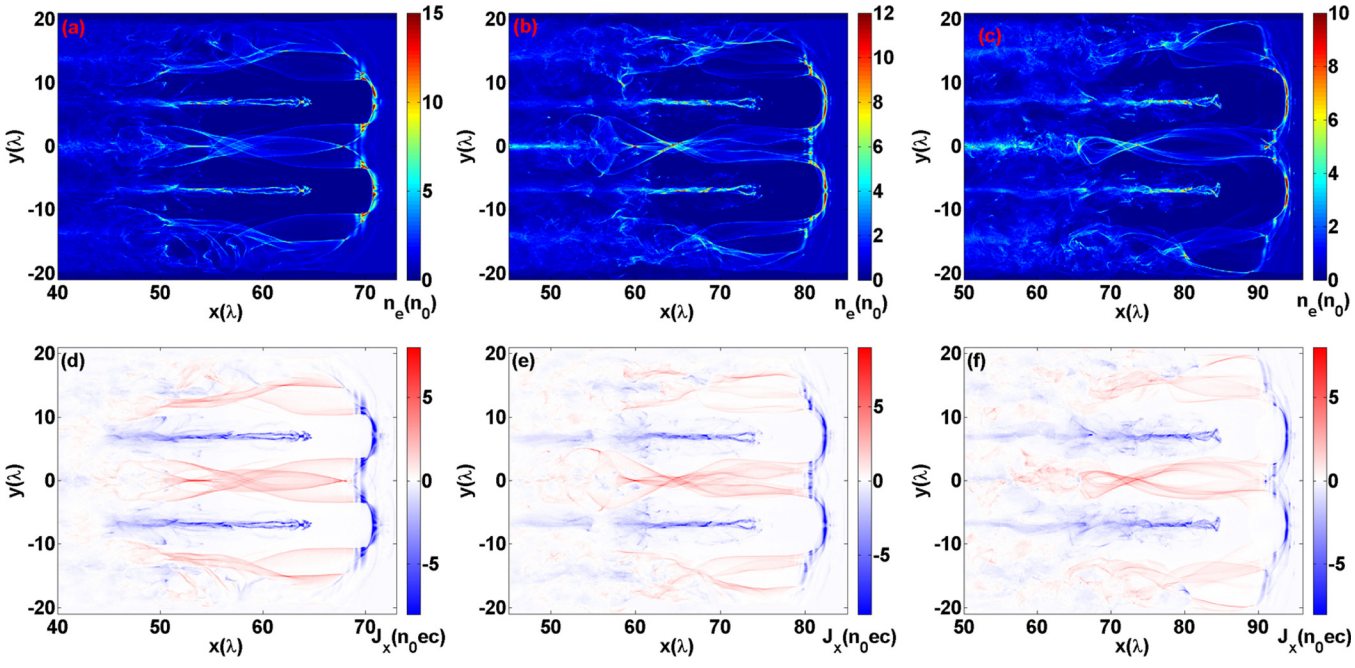

FIG. 2. (a)–(c) The electron density distribution at 75 T_0, 87 T_0, and 99 T_0, respectively. (d)–(f) The corresponding current density distribution.

This article is copyrighted as indicated in the article. Reuse of AIP content is subject to the terms at: http://scitation.aip.org/termsconditions. Downloaded to IP: 61.86.248.29 On: Mon, 19 Oct 2015 20:10:37

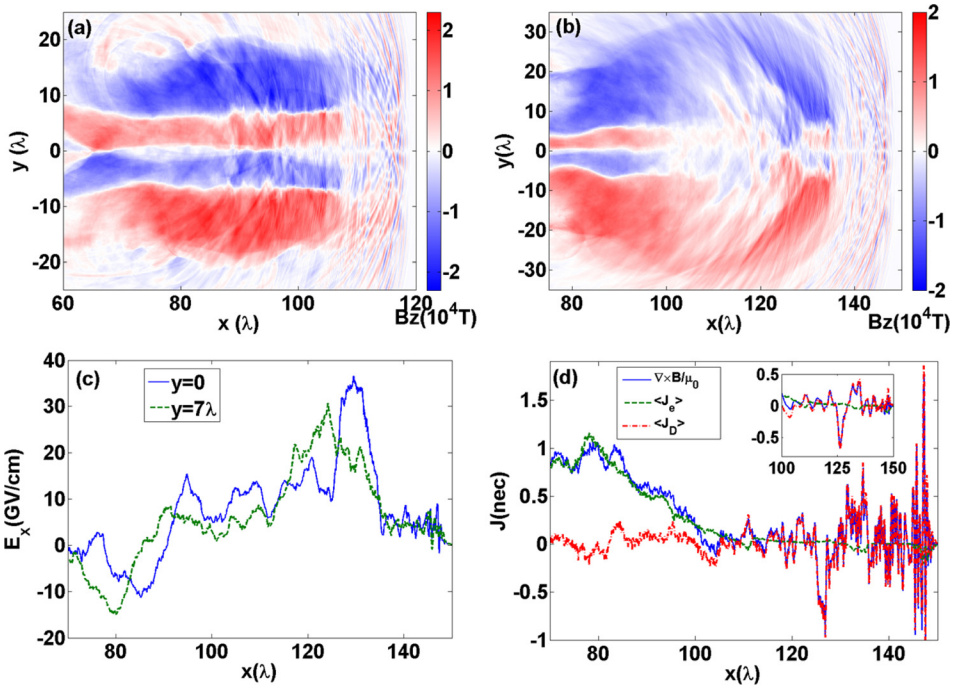

FIG. 3. (a) and (b) The z-component of the magnetic field (B_z) distribution at 123 T_0 and 153 T_0. (c) The longitudinal electric field along $y=0$ (blue solid line) and $y=7\lambda$ (green dashed line) at 153 T_0. (d) The contributions of terms in Ampère-Maxwell equation at 153 T_0, which are spatial averaged over the current sheet ($-\lambda < y < \lambda$): $\frac{1}{\mu_0}\langle \nabla \times \mathbf{B}\rangle_x$ (blue), the convection current density $\langle \mathbf{J_e}\rangle_x$ (green), and the displacement current density $\langle \mathbf{J_D}\rangle_x$ (red). Inset: The smoothed value near the region where the inductive electric field grows.

the magnetic fields B_z, i.e., it flows in the x direction. This is analogous to a current sheet formation during magnetic reconnection in the vicinity of the X-line, where the opposite magnetic field lines reconnect rearranging the magnetic field topology.[66] In Fig. 3(c), we plot the longitudinal electric field profiles along the current sheet ($y=0$) and along one of the laser axes ($y=7\lambda$) at 153 T_0. Before the moment shown in Fig. 3(c), the typical value of E_x in the current sheet is as high as the plasma wave magnitude: $E_0 = cm_e\omega_p/e \approx 10$ GV/cm. During the magnetic field annihilation, the E_x quickly increases up to 35 GV/cm in the current sheet, seen in Fig. 3(c). At the same time, the peak of E_x located in the wake wave is about 30 GV/cm along the laser axis. Thus, the inductive electric field generated by magnetic field annihilation is stronger than the charge separation field.

In Fig. 3(c), the localization of the strong inductive electric field is beyond the initial plasma target; the electron density in this region is very low, in contrast to the case considered by Ping *et al.*,[58] where the magnetic field dissipation takes place at relatively high electron density inside the target.

In Fig. 3(d), we plot all the terms in Ampère-Maxwell equation, Eq. (3) along the central axis ($y=0$) at 153 T_0: the x component of the curl of the magnetic field, $\mu_0^{-1}\langle \nabla \times \mathbf{B}\rangle_x$, the convection electric current density $\langle \mathbf{J_e}\rangle_x = -en\mathbf{v}_x$, and the displacement current $\langle \mathbf{J_D}\rangle_x = \varepsilon_0 \partial_t E_x$. In the region corresponding to a strong inductive field ($125\lambda < x < 135\lambda$), the conventional current is negligible while the term of $\mu_0^{-1}\langle \nabla \times \mathbf{B}\rangle_x$ is almost the same as $\langle \mathbf{J_D}\rangle_x = \varepsilon_0 \partial_t E_x$ (see also spatially smoothed curves in the inset of Fig. 3(d)). Thus, it is the displacement current that balances the curl of the magnetic field. We conclude that magnetic field annihilation generates a strong inductive electric field, represented in Ampère-Maxwell equation, Eq. (3), by the displacement current.

The inductive electric field generated in the current sheet accelerates charged particles. In this way, the magnetic field energy is converted into the kinetic energy of plasma. The acceleration of electrons is seen in Fig. 4. In our case, the inductive electric field represented by the E_x component is positive; therefore, it accelerates electrons in the negative direction of the x-axis. Electrons outside the current sheet are accelerated by the wakefield. This is seen in the electron momentum spectra in Figs. 4(a) and 4(b), for $t = 69\,T_0$ and 138 T_0, respectively, where central electrons reside in the current sheet ($-2\lambda < y < 2\lambda$) and side electrons are from the interval of $8\lambda < y < 25\lambda$. At $t = 69\,T_0$, well before magnetic field annihilation, the maximum momentum of side electrons is larger than that of central electrons. Here, the electrons near the central axis reside in the overlapping shells of bubbles created by two parallel laser pulses. They form a return current on the second half of the Langmuir oscillation. At 138 T_0, during magnetic field annihilation, the magnitude of the negative longitudinal momentum of central electrons quickly exceeds twice that of the side electrons. In Fig. 4, in frames (c), (d) at 69 T_0, and (e), (f) at 138 T_0, we present the momentum spaces (x, p_x) and (y, p_x) for all electrons. At 69 T_0, two positive peaks in frame (c) correspond to the electrons accelerated directly by the laser field (near $x = 65\lambda$) and by the wakefield (closer to $x = 50\lambda$), whereas wide arcs in frame (d) are formed by electrons with negative longitudinal momenta on the second half of the Langmuir oscillation. At 138 T_0, a pillar formed by electrons with negative longitudinal momenta seen in frame (f) corresponds to the acceleration in the current sheet. Those electrons are located in the interval of $80\lambda < x < 100\lambda$ as seen in frame (e), in agreement with the location of magnetic field annihilation presented above. We also notice that positive momenta in the current sheet are much less than the magnitudes of negative longitudinal momenta, frame (f). This fact, together with the

This article is copyrighted as indicated in the article. Reuse of AIP content is subject to the terms at: http://scitation.aip.org/termsconditions. Downloaded to IP: 61.86.248.29 On: Mon, 19 Oct 2015 20:10:37

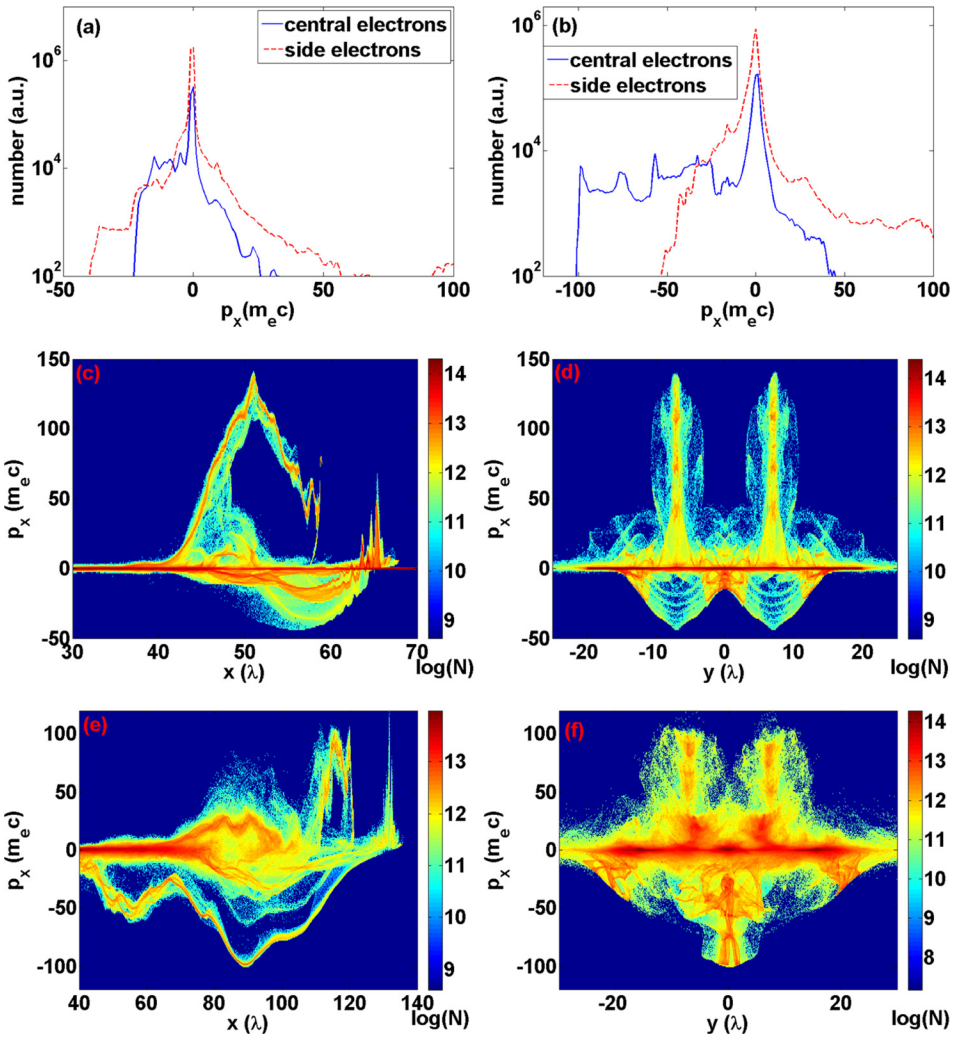

FIG. 4. The longitudinal momentum distribution comparison between current sheet electrons and side electrons at $t = 69\,T_0$ and 138 T_0 are plotted in (a) and (b), respectively. (c) and (d) The electron momentum space $x - p_x$ and $y - p_x$ at 69 T_0, respectively. (e) and (f) The corresponding phase space at 138 T_0. The color bars represent the particle numbers in logarithmic scale.

characteristic distribution of negative longitudinal momenta in frame (e), excludes a Coulomb explosion of the current sheet as a possible mechanism explaining the backward acceleration. We conclude that backward electron acceleration in the current sheet is due to the inductive electric field generated via magnetic field annihilation.

In the transverse direction, the motion of backward accelerated electrons is influenced by both the E_y and B_z component. We define the effective transverse field as $F_y \mathrm{e}_y = E_y \mathrm{e}_y + v_x \mathrm{e}_x \times B_z \mathrm{e}_z$, where e_x, e_y, and e_z are the unit vectors along the x, y, and z axes, respectively. Since the backward electron speed is close the light speed, $v_x \approx -c$, we can redefine the effective transverse field as $F_y = E_y + cB_z$. This quantity is shown in Figs. 5(a) and 5(c) at 87 T_0 and 138 T_0, respectively. It is seen that the transverse field focuses backward accelerated electrons in the current sheet. Fig. 5(b) demonstrates the momentum space (p_x, p_y) of all electrons at 87 T_0, before the rise of the inductive electric field. The maximum negative longitudinal momentum corresponds to electrons in the wakefield. At 138 T_0, Fig. 5(d), electrons appear to be backward accelerated by the inductive electric field. They form a bunch with $p_x \approx -100 m_e c$ and relatively small transverse momentum, as compared to Fig. 5(b). This indicates the focusing effect of the effective transverse field on the backward accelerated electrons in the current sheet.

B. Magnetic field energy conversion

Here, we analyze the evolution of the magnetic field and longitudinal electric field energy in order to confirm the energy transfer from a large-scale magnetic field to a well-localized electric field. The energy stored in the z-component of the magnetic field, $|B_z|^2$, is integrated in the whole simulation box and plotted in Figs. 6(a) and 6(c) as a function of time for three cases: (1) the simulation with two laser pulses discussed above (labeled as "Two Pulses," solid line), (2) the simulation with only a single laser pulse and the same target (labeled as "Single Pulse," dotted line), and (3) the simulation with two pulses initially separated by 40λ along the y-axis, larger separation than in the above-discussed simulation, and the target with transverse size enlarged to 66λ (labeled as "Large Separation," dashed line). Similarly, we plot the evolution of longitudinal electric field energy $|E_x|^2$ for these cases in Figs. 6(b) and 6(d). For the case of a single pulse, we also show energy values multiplied by two, which corresponds to a case of two pulses with infinitely large initial transverse separation.

This article is copyrighted as indicated in the article. Reuse of AIP content is subject to the terms at: http://scitation.aip.org/termsconditions. Downloaded to IP: 61.86.248.29 On: Mon, 19 Oct 2015 20:10:37

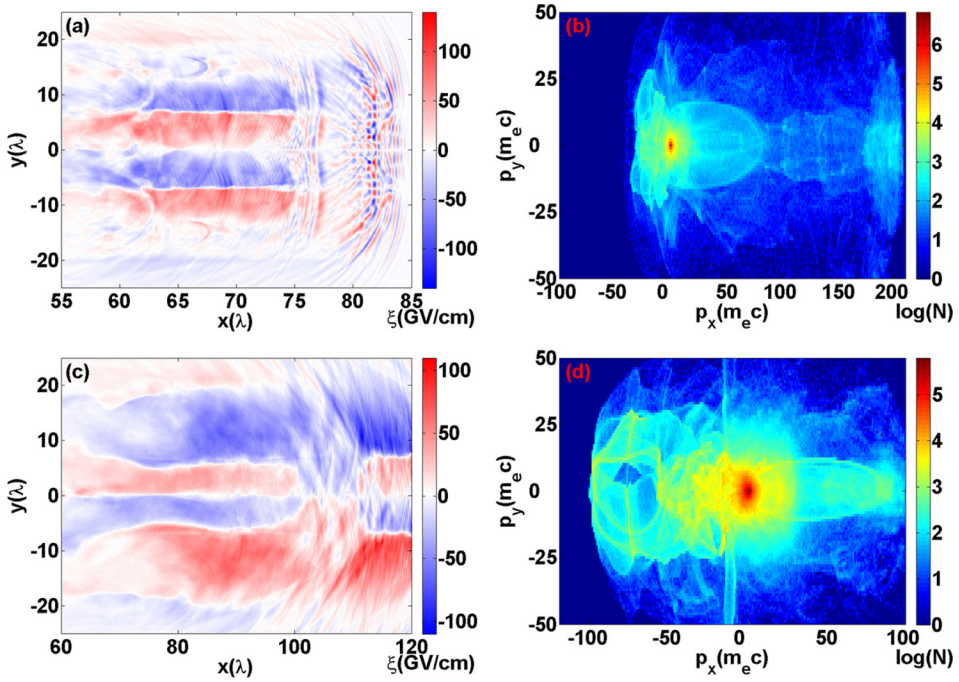

FIG. 5. The effective transverse fields $F_y = E_y + cB_z$ at 87 T_0 and 138 T_0 are plotted in (a) and (c), respectively. The corresponding momentum space is shown in (b) and (d). The color bars in (b) and (d) represent the particle numbers in logarithm scale.

If there was no interaction between the laser pulses, the solid curve ("Two Pulses") would follow the dashed curve ("Single Pulse" $\times 2$). As seen in Fig. 6(a), the pulses start to interact at about 60 T_0. In terms of electric field energy, Fig. 6(b), a deviation between the curves grows after 90 T_0 and becomes significant at about 110 T_0; starting from 110 T_0 to 145 T_0 the solid curve exceeds the dashed one. At the same time, the magnetic field energy in the case of "Two Pulses" decreases in comparison with the case of "Single Pulse" ($\times 2$). This indicates magnetic annihilation in the simulation box.

With a larger separation between the laser pulses, the magnetic field annihilation occurs later in time, because more time is necessary for magnetic dipoles expansion before they can touch. This case is shown in Figs. 6(c) and 6(d). The deviation between solid and dashed curves in Fig. 6(c) begins from about 125 T_0, while the longitudinal electric field energy exceeds that in the case of "Single Pulse" at about 140 T_0, Fig. 6(d). Compared with the previous case of less separation between pulses, the time delay in the large separation case is about 35 T_0, determined by the laser pulse diffraction and the plasma density gradient.

C. Magnetic annihilation with nonequal laser pulses

In this subsection, we demonstrate magnetic field annihilation using two parallel laser pulses with different laser

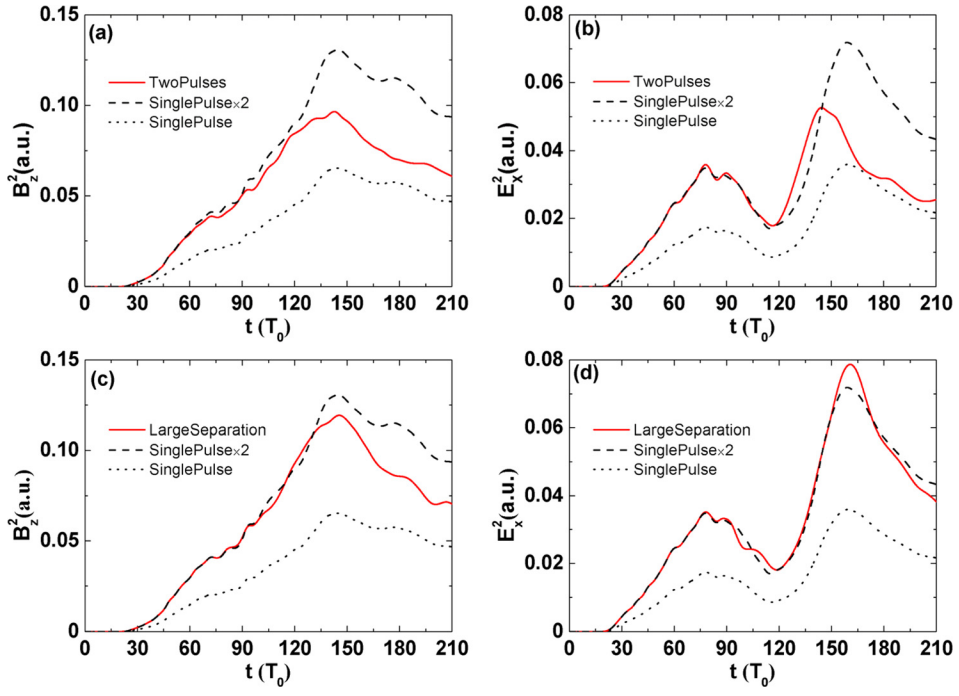

FIG. 6. The evolution of total $|B_z|^2$ and $|E_x|^2$ in the simulation box for 3 cases is plotted in (a) and (b). The red line, black solid line, and black dashed line represent the cases of two-pulses, single-pulse, and mathematically double single-pulse. (c) and (d) The corresponding evolution for the two pulses with large separation. The electric field energy and magnetic field energy are in arbitrary unit.

This article is copyrighted as indicated in the article. Reuse of AIP content is subject to the terms at: http://scitation.aip.org/termsconditions. Downloaded to IP: 61.86.248.29 On: Mon, 19 Oct 2015 20:10:37

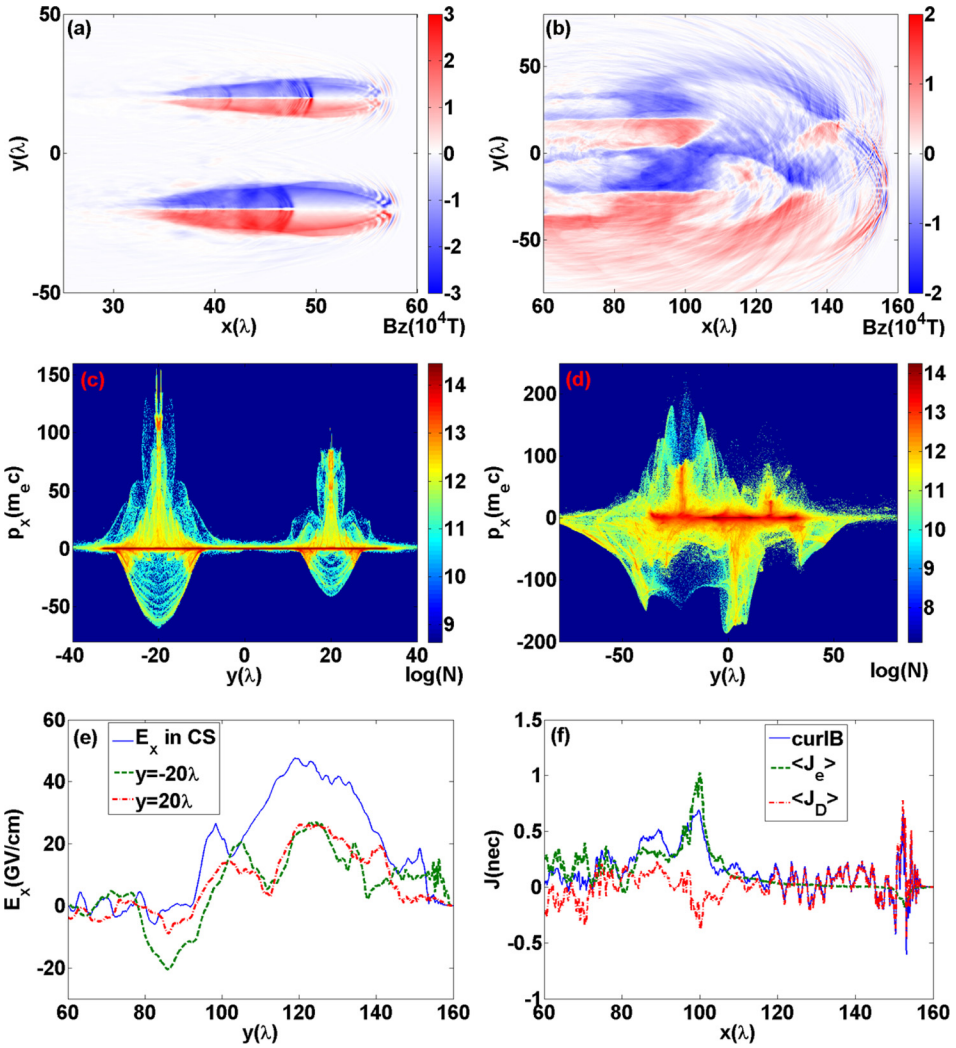

FIG. 7. (a) and (b) The z-component of the magnetic field (B_z) distribution at 60 T_0 and 162 T_0. (c) and (d) The electron $y - p_x$ distribution at 60 T_0 and 162 T_0. (e) The longitudinal electric field profiles at 162 T_0 along current sheet (blue solid line), weak laser axis ($y = 20\lambda$) (green dashed line), and strong laser axis ($y = -20\lambda$) (red dash-dotted line). (f) The contributions of terms in Faraday's law at 162 T_0.

intensities. The plasma target is the same as in Section II. Two pulses with the intensity of 10^{21} W/cm^2 and 5×10^{21} W/cm^2 are focused onto the target left boundary. The optical axes of the pulses are at $y = \pm 20\,\lambda$. Fig. 7(a) shows two magnetic dipoles with different transverse sizes formed in the density plateau at $t = 60\,T_0$. According to Eqs. (4) and (5), the high intensity pulse at $y = -20\,\lambda$ creates a larger and stronger magnetic dipole; the size and strength of magnetic field seen in the simulation are well consistent with the prediction of those equations. The corresponding electron momentum space (y, p_x) is plotted in Fig. 7(c). We see the trapped accelerated electrons with positive momentum and return electrons with negative longitudinal momentum corresponding to two bubbles with different wakefields. As in the cases discussed above, the magnetic dipoles propagating in the downramp expand and start to annihilate. Since the magnetic field strengths of the two dipoles are not equivalent, the weaker magnetic field is completely canceled by the stronger one as shown in the B_z distribution at 162 T_0 in Fig. 7(b). Accordingly, the current sheet shifts in the y-direction. The electrons backward accelerated by the inductive electric field also shifts with the current sheet, as seen in the momentum space (y, p_x) in Fig. 7(d). The magnitude of the negative longitudinal momentum of these electrons reaches almost $200\,m_e c$, twice as great as in Fig. 4(f), and similar to the positive momentum of the electrons trapped and accelerated in the wakefield in the forward direction. The longitudinal electric field profiles in the current sheet and along the two optical axes of laser pulses are plotted in Fig. 7(e). The inductive electric field strength reaches 50 GV/cm, much stronger than in Fig. 3(c). By analyzing the contributions of terms in Ampère-Maxwell equation, Fig. 7(f), we find the location of the strong inductive field, $120\,\lambda < x < 140\,\lambda$, corresponding to the region where the conventional current is negligible. As in previous cases, the variation of magnetic field is compensated by the displacement current and converts to the longitudinal electric field, which accelerates electrons backward.

D. Magnetic annihilation in high density plasma with high intensity laser pulses

The transparency of the plasma depends on the electromagnetic wave amplitude, due to relativistic effects.[27] Ultra-intense laser pulses can propagate in near-critical or overdense plasma creating bubble structures with the magnetic dipole. The interaction of such magnetic dipoles generated by two parallel laser pulses will cause magnetic annihilation similar to the cases considered above.

This article is copyrighted as indicated in the article. Reuse of AIP content is subject to the terms at: http://scitation.aip.org/termsconditions. Downloaded to IP: 61.86.248.29 On: Mon, 19 Oct 2015 20:10:37

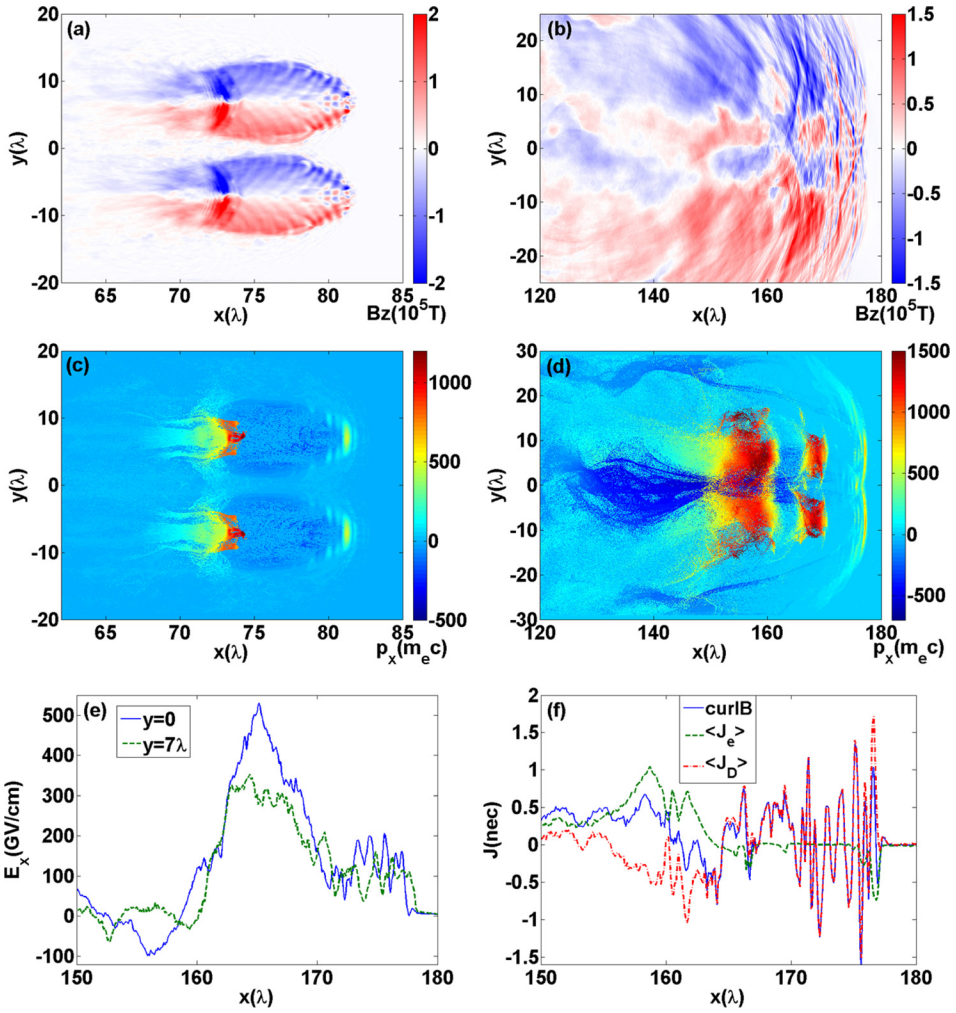

FIG. 8. (a) and (b) The z-component of the magnetic field (B_z) distribution at 84 T_0 and 184 T_0. (c) and (d) The electron maximum momentum distribution at 84 T_0 and 184 T_0. (e) The longitudinal electric field profiles at 184 T_0 along current sheet (blue solid line), laser axis ($y = 7\lambda$) (green dashed line). (f) The contributions of terms in Ampère-Maxwell equation at 184 T_0.

We present a simulation, where the plasma is located in the interval from 60λ to 162λ along the x-axis, with the peak density of n_c. The target profile has a sharp edge with the width of 2λ, a plateau spanning 40λ, and a long downramp with a length of 60λ. The intensity of each laser pulse is 10^{23} W/cm^2. The separation between the laser pulses is 14λ. The generated magnetic field strength is about 2×10^5 T, as estimated with Eq. (5), in agreement with the B_z distribution at 84 T_0 in Fig. 8(a). The processes of magnetic dipole expansion and opposite magnetic field annihilation are analogous to the cases discussed above, as seen in Fig. 8(b). In contrast to previous cases, the electron acceleration in the current sheet is much more intense. In Figs. 8(c) and 8(d), we show the distribution of the electron momentum x-component, p_x, in the (x, y) plane at 84 T_0 and 184 T_0, respectively. The magnitude of the electron negative longitudinal momentum in the current sheet reaches $700\,m_ec$, i.e., 350 MeV, as seen in Fig. 8(d). The corresponding electrons are accelerated by the strong inductive field generated during magnetic annihilation. This field is shown at 184 T_0 in Fig. 8(e) by the solid curve. It is greater than the wakefields along the optical axes of the laser pulses in the interval of 163λ to 170λ, which corresponds to the region where the displacement current predominantly balances the curl of magnetic field, as shown in Fig. 8(f).

IV. CONCLUSIONS

We demonstrate fast magnetic dissipation via magnetic field annihilation driven by two parallel intense femtosecond laser pulses co-propagating in underdense plasma, with the help of 2.5D PIC simulations. Two laser pulses create magnetic dipoles, which gradually expand in the transverse direction while the laser pulses are co-propagating. If the transverse separation between laser pulses is small enough, the expanding dipoles collide along the central axis between the laser pulses. At this axis, a current sheet is formed, initially sustaining the magnetic field. When the transverse gradient of the magnetic field increases and the laser pulses enter a region with decreasing plasma density (the downramp), the electric current can no longer sustain the magnetic field. The oppositely directed magnetic fields annihilate at the central axis, creating an inductive longitudinal electric field. We show that at this time the displacement current balances the curl of the magnetic field. The inductive longitudinal electric field generated in the vicinity of the current sheet efficiently accelerates charged particles; in particular, it accelerates electrons in the direction opposite to the laser propagation. We found that unequal laser pulses can also produce energetic backward accelerated electrons. We show that with laser pulses reaching the intensity of 10^{23} W/cm^2 it is possible to

This article is copyrighted as indicated in the article. Reuse of AIP content is subject to the terms at: http://scitation.aip.org/termsconditions. Downloaded to IP: 61.86.248.29 On: Mon, 19 Oct 2015 20:10:37

realize the discussed regimes of magnetic field annihilation in near-critical or overdense plasma, which gives more efficient particle acceleration by the inductive electric field.

Our results open a way for experimental realization of new relativistic regimes of fast magnetic field dissipation, where large-scale magnetic field energy is converted to the energy of collimated bunches of fast charged particles. If two intense femtosecond laser pulses can be well synchronized, or a single laser pulse can be formed with an intensity drop at the central axis or plane, the above-discussed regimes can be realized with a self-replenishable gas jet or an easily available foam targets. Ultra-intense regimes of fast magnetic field dissipation with high energy conversion rates can be demonstrated in the future using multi-petawatt laser facilities such as ELI-Beamlines.[59]

ACKNOWLEDGMENTS

This work was supported by the ELI (Project No. CZ.1.05/1.1.00/02.0061). Computational resources were provided by the MetaCentrum under the Program No. LM2010005 and by IT4Innovations Centre of Excellence under Project Nos. CZ.1.05/1.1.00/02.0070 and LM2011033. The EPOCH code was developed as part of the UK EPSRC funded Project No. EP/G054940/1.

[1]J. B. Taylor, Rev. Mod. Phys. **58**, 741 (1986).
[2]E. G. Zweibel and M. Yamada, Annu. Rev. Astron. Astrophys. **47**, 291 (2009).
[3]M. Yamada, R. Kulsrud, and H. Ji, Rev. Mod. Phys. **82**, 603 (2010).
[4]D. Biskamp, *Magnetic Reconnections in Plasmas* (Cambridge University Press, Cambridge, England, 2000).
[5]S. Masuda, T. Kosugi, H. Hara, S. Tsuneta, and Y. Ogawara, Nature **371**, 495 (1994).
[6]J. Goodman and D. Uzdensky, Astrophys. J. **688**, 555 (2008).
[7]M. A. Yates, D. B. van Hulsteyn, H. Rutkowski, G. Kyrala, and J. U. Brackbill, Phys. Rev. Lett. **49**, 1702 (1982).
[8]E. N. Parker, J. Geophys. Res. **62**, 509, doi:10.1029/JZ062i004p00509 (1957).
[9]R. P. Lin, S. Krucker, G. J. Hurford, D. M. Smith, H. S. Hudson, G. D. Holman, R. A. Schwartz, B. R. Dennis, G. H. Share, R. J. Murphy *et al.*, Astrophys. J. Lett. **595**, L69 (2003).
[10]Y. Su, A. M. Veronig, G. D. Holman, B. R. Dennis, T. J. Wang, M. Temmer, and W. Q. Gan, Nat. Phys. **9**, 489 (2013).
[11]R. L. Fermo, M. Opher, and J. F. Drake, Phys. Rev. Lett. **113**, 031101 (2014).
[12]Q. Jiong, W. Haimin, C. Z. Cheng, and E. G. Dale, Astrophys. J. **604**, 900 (2004).
[13]M. Faganello, F. Califano, F. Pegoraro, T. Andreussi, and S. Benkadda, Plasma Phys. Controlled Fusion **54**, 124037 (2012).
[14]P. Brady, T. Ditmire, W. Horton, M. L. Mays, and Y. Zakharov, Phys. Plasmas **16**, 043112 (2009).
[15]D. Giannios, Mon. Not. R. Astron. Soc.: Lett. **408**, L46 (2010).
[16]Z. Bing and Y. Huirong, Astrophys. J. **726**, 90 (2011).
[17]J. C. McKinney and D. A. Uzdensky, Mon. Not. R. Astron. Soc. **419**, 573 (2012).
[18]C. Benoit, A. U. Dmitri, and C. B. Mitchell, Astrophys. J. **746**, 148 (2012).
[19]M. Yamada, F. M. Levinton, N. Pomphrey, R. Budny, J. Manickam, and Y. Nagayama, Phys. Plasmas **1**, 3269 (1994).
[20]R. J. Hastie, Astrophys. Space Sci. **256**, 177 (1997).
[21]D. Biskamp, Phys. Fluids **29**, 1520 (1986).
[22]J. F. Drake, R. G. Kleva, and M. E. Mandt, Phys. Rev. Lett. **73**, 1251 (1994).
[23]H. Ji, M. Yamada, S. Hsu, and R. Kulsrud, Phys. Rev. Lett. **80**, 3256 (1998).
[24]S. V. Bulanov, T. Z. Esirkepov, D. Habs, F. Pegoraro, and T. Tajima, Eur. Phys. J. D **55**, 483 (2009).
[25]S. V. Bulanov, T. Z. Esirkepov, M. Kando, J. Koga, K. Kondo, and G. Korn, Plasma Phys. Rep. **41**, 1 (2015).
[26]D. Strickland and G. Mourou, Opt. Commun. **56**, 219 (1985).
[27]G. A. Mourou, T. Tajima, and S. V. Bulanov, Rev. Mod. Phys. **78**, 309 (2006).
[28]G. A. Askar'yan, S. V. Bulanov, F. Pegoraro, and A. M. Pukhov, Comments Plasma Phys. Controlled Fusion **17**(1), 35 (1995).
[29]P. M. Nilson, L. Willingale, M. C. Kaluza, C. Kamperidis, S. Minardi, M. S. Wei, P. Fernandes, M. Notley, S. Bandyopadhyay, M. Sherlock *et al.*, Phys. Rev. Lett. **97**, 255001 (2006).
[30]C. K. Li, F. H. Seguin, J. A. Frenje, J. R. Rygg, R. D. Petrasso, R. P. J. Town, O. L. Landen, J. P. Knauer, and V. A. Smalyuk, Phys. Rev. Lett. **99**, 055001 (2007).
[31]J. Zhong, Y. Li, X. Wang, J. Wang, Q. Dong, C. Xiao, S. Wang, X. Liu, L. Zhang, L. An *et al.*, Nat. Phys. **6**, 984 (2010).
[32]Q.-L. Dong, S.-J. Wang, Q.-M. Lu, C. Huang, D.-W. Yuan, X. Liu, X.-X. Lin, Y.-T. Li, H.-G. Wei, J.-Y. Zhong *et al.*, Phys. Rev. Lett. **108**, 215001 (2012).
[33]T. Nakamura and S. Kawata, Phys. Rev. E **67**, 026403 (2003).
[34]S. Kawata, T. Izumiyama, T. Nagashima, M. Takano, D. Barada, Q. Kong, Y. J. Gu, P. X. Wang, Y. Y. Ma, and W. M. Wang, Laser Ther. **22**, 103 (2013).
[35]S.-Q. Liu, X.-S. Yang, and X.-Q. Li, Phys. Plasmas **18**, 112109 (2011).
[36]Q. L. Dong, D. W. Yuan, S. J. Wang, Y. T. Li, X. Liu, S. E. Jiang, Y. K. Ding, K. Du, M. Y. Yu, X. T. He *et al.*, J. Plasma Phys. **78**, 497 (2012).
[37]Y. Ono, H. Tanabe, T. Yamada, M. Inomoto, T. Ii, S. Inoue, K. Gi, T. Watanabe, M. Gryaznevich, R. Scannell *et al.*, Plasma Phys. Controlled Fusion **54**, 124039 (2012).
[38]Q. Dong, D. Yuan, S. Wang, X. Liu, Y. Li, X. Lin, H. Wei, J. Zhong, S. Jiang, Y. Ding *et al.*, High Power Laser Sci. Eng. **1**, 11 (2013).
[39]G. Fiksel, W. Fox, A. Bhattacharjee, D. H. Barnak, P. Y. Chang, K. Germaschewski, S. X. Hu, and P. M. Nilson, Phys. Rev. Lett. **113**, 105003 (2014).
[40]G. W. Inverarity and E. R. Priest, Phys. Plasmas **3**, 3591 (1996).
[41]J. F. Drake, D. Biskamp, and A. Zeiler, Geophys. Res. Lett. **24**, 2921, doi:10.1029/97GL52961 (1997).
[42]J. D. Huba and L. I. Rudakov, Phys. Rev. Lett. **93**, 175003 (2004).
[43]J. Yoo, M. Yamada, H. Ji, and C. E. Myers, Phys. Rev. Lett. **110**, 215007 (2013).
[44]J. G. Kirk, Phys. Rev. Lett. **92**, 181101 (2004).
[45]M. Hoshino, T. Mukai, T. Terasawa, and I. Shinohara, J. Geophys. Res.: Space Phys. **106**, 25979 (2001).
[46]S. Zenitani and M. Hoshino, Astrophys. J. Lett. **562**, L63 (2001).
[47]M. A. Shay, J. F. Drake, and M. Swisdak, Phys. Rev. Lett. **99**, 155002 (2007).
[48]W. Fox, A. Bhattacharjee, and K. Germaschewski, Phys. Rev. Lett. **106**, 215003 (2011).
[49]H. Che, J. F. Drake, and M. Swisdak, Nature **474**, 184 (2011).
[50]G. Baumann and A. Nordlund, Astrophys. J. Lett. **759**, L9 (2012).
[51]W. Fox, A. Bhattacharjee, and K. Germaschewski, Phys. Plasmas **19**, 056309 (2012).
[52]B. Naoki and A. Bhattacharjee, Astrophys. J. **750**, 129 (2012).
[53]Z. C. Zhang, Q. M. Lu, Q. L. Dong, S. Lu, C. Huang, M. Y. Wu, Z. M. Sheng, S. Wang, and J. Zhang, Chin. Phys. Lett. **30**, 045201 (2013).
[54]S. Lu, Q. Lu, Q. Dong, C. Huang, S. Wang, J. Zhu, Z. Sheng, and J. Zhang, Phys. Plasmas **20**, 112110 (2013).
[55]F. Guo, H. Li, W. Daughton, and Y.-H. Liu, Phys. Rev. Lett. **113**, 155005 (2014).
[56]M. Melzani, R. Walder, D. Folini, C. Winisdoerffer, and J. M. Favre, Astron. Astrophys. **570**, A111 (2014).
[57]V. Olshevsky, G. Lapenta, and S. Markidis, Phys. Rev. Lett. **111**, 045002 (2013).
[58]Y. L. Ping, J. Y. Zhong, Z. M. Sheng, X. G. Wang, B. Liu, Y. T. Li, X. Q. Yan, X. T. He, J. Zhang, and G. Zhao, Phys. Rev. E **89**, 031101 (2014).
[59]G. Mourou, G. Korn, W. Sandner, and J. Collier, *ELI Extreme Light Infrastructure (Whitebook)* (THOSS Media GmbH, Berlin, Germany, 2011).
[60]C. P. Ridgers, J. G. Kirk, R. Duclous, T. G. Blackburn, C. S. Brady, K. Bennett, T. D. Arber, and A. R. Bell, J. Comput. Phys. **260**, 273 (2014).
[61]P. Sprangle, E. Esarey, A. Ting, and G. Joyce, Appl. Phys. Lett. **53**, 2146 (1988).
[62]G. A. Askar'yan, S. V. Bulanov, F. Pegoraro, and A. M. Pukhov, JETP Lett. **60**(4), 251 (1994).
[63]J. Nycander and M. B. Isichenko, Phys. Fluids B **2**, 2042 (1990).
[64]S. K. Yadav, A. Das, and P. Kaw, Phys. Plasmas **15**, 062308 (2008).
[65]V. E. Zakharov and E. A. Kuznetsov, Phys. Usp. **40**, 1087 (1997).
[66]S. I. Syrovatskii, Sov. Phys. JETP **33**(5), 933 (1971).

This article is copyrighted as indicated in the article. Reuse of AIP content is subject to the terms at: http://scitation.aip.org/termsconditions. Downloaded to IP: 61.86.248.29 On: Mon, 19 Oct 2015 20:10:37